PCCP

PAPER

View Article Online
View Journal | View Issue

Cite this: *Phys. Chem. Chem. Phys.*, 2014, **16**, 2048

Insight into band positions and inter-particle electron transfer dynamics between CdS nanoclusters and spatially isolated TiO_2 dispersed in cubic MCM-48 mesoporous materials: a highly efficient system for photocatalytic hydrogen evolution under visible light illumination†

Rui Peng,[a] Cuikun Lin,[a] Jonas Baltrusaitis,[b] Chia-Ming Wu,[a] Nada M. Dimitrijevic,[c] Tijana Rajh,[c] Stanley May[a] and Ranjit T. Koodali*[a]

CdS incorporated Si-MCM-48 and Ti-MCM-48 cubic phased mesoporous photocatalysts were prepared by a two-step modification synthetic approach under relatively mild conditions. A highly efficient (24.8%, apparent quantum yield (AQY)) photocatalyst for visible light (λ > 400 nm) enabled solar hydrogen evolution can be realized by assembling CdS with Ti-MCM-48 cubic mesoporous materials in the *absence* of a noble metal co-catalyst. The photocatalytic mechanism was thoroughly investigated and demonstrated by conducting a wealth of characterization techniques such as powder X-ray diffraction (XRD), nitrogen adsorption isotherm, transmission electron microscopy (TEM), UV-visible diffuse reflectance spectroscopy (DRS), X-ray photoelectron spectroscopy (XPS), ultraviolet photoelectron spectroscopy (UVPS), atomic absorption spectroscopy (AAS), photoluminescence (PL) spectroscopy, time-resolved fluorescence emission decay, and electron paramagnetic resonance (EPR) spectroscopy studies. This work is the first to unambiguously identify the band positions of both CdS and TiO_2 encapsulated in porous materials. The photocatalytic activity of the CdS incorporated Ti-MCM-48 mesoporous photocatalysts was found to be dependent on the content of both CdS and TiO_2. A correlation between the electron injection efficiency and the photocatalytic activity was established as well in the CdS incorporated Ti-MCM-48 mesoporous photocatalysts.

Received 4th July 2013,
Accepted 18th November 2013

DOI: 10.1039/c3cp52801d

www.rsc.org/pccp

1. Introduction

Hydrogen generation from water by effective use of solar energy serves as an ideal model for an ultimate "green" energy system. This scenario (albeit in a photoelectrochemical mode) was first realized by Fujishima and Honda from the decomposition of water by using a TiO_2 photoelectrode and Pt as a counter-electrode under UV light illumination in 1972.[1] Inspired by this ground-breaking work, a number of research studies, along with a myriad of semiconductor photocatalysts, have been explored in this field for the past few decades.[2–7]

Titanium dioxide has been extensively studied for hydrogen evolution from photocatalytic splitting of water due to its ease of preparation and excellent stability towards UV light.[7] However, bare TiO_2 photocatalysts show little or no photocatalytic activity for hydrogen evolution primarily due to their unfavorable conduction band edge position and rapid recombination of the photogenerated electron–hole pairs. Extensive efforts have been devoted to develop strategies to minimize the recombination of charge carriers and several key factors have emerged. First, it has been proven that the crystallinity of the TiO_2 species is paramount to their photocatalytic performance.[8,9] In addition, the particle size of TiO_2 is an important factor that has great impact on the photocatalytic activity.[10]

In recent years, titania species have been incorporated into periodic mesoporous materials that have large surface areas and long-range uniform pore diameters.[11–13] It has been found that spatially isolated Ti^{4+} ions in tetrahedral coordination show higher photocatalytic activity compared to bulk TiO_2, in which the Ti^{4+} ions are in octahedral coordination. The superior photocatalytic

[a] *Department of Chemistry, University of South Dakota, Vermillion, South Dakota 57069, USA. E-mail: Ranjit.Koodali@usd.edu; Fax: +1-605-677-6397; Tel: +1-605-677-6189*
[b] *Photocatalytic Synthetic Group, University of Twente, The Netherlands*
[c] *Nanoscience and Nanotechnology, and Chemical Sciences and Engineering Division, Argonne National Laboratory, Argonne, Illinois 60439, USA*

† Electronic supplementary information (ESI) available. See DOI: 10.1039/c3cp52801d

activity of tetrahedrally coordinated Ti^{4+} ions can be ascribed to the ligand-to-metal charge-transfer (LMCT) from O^{2-} to Ti^{4+}. This process can be presented as $[Ti^{4+}–O^{2-}] \rightarrow [Ti^{3+}–O^{-}]^*$ in which the photogenerated electron–hole pairs are localized next to each other. These long-lived electron–hole pairs have a lower tendency to undergo charge-carrier recombination than in bulk TiO_2. Hence, the photocatalytic activity of highly dispersed and spatially isolated titania species is enhanced compared to bulk TiO_2 semiconductors.[14,15]

A big drawback of photocatalysts containing Ti^{4+} ions in tetrahedral coordination is that these materials can be employed as catalysts only under UV or near UV light owing to their large bandgap energy. Hence, these materials use only a fraction of the solar spectrum. In order to improve the photocatalytic efficiency, photocatalysts that can capture visible light from the solar spectrum need to be designed. Among a handful of visible light driven photocatalysts,[16,17] CdS is widely used because of its ease of preparation and versatility in photocatalysis.[18–20] However, a big drawback of CdS is the drastic corrosion that takes place during photocatalytic processes. As a consequence, photocatalytic activity dramatically decreases, thereby restricting the application of CdS based photocatalysts.[21,22] Photocorrosion of CdS can be minimized by using sulfide and/or sulfite salts as sacrificial reagents in photocatalytic procedures.[19,23] Other methods have been evaluated to enhance the stability and activity of CdS based photocatalysts. For instance, coupling CdS with another semiconductor has proven to be a promising strategy.[24,25]

Embedding CdS into micro- or mesoporous materials is a prominent approach for increasing the overall photocatalytic efficiency and for strengthening the stability of CdS moieties.[26,27] First, CdS species can be confined within the uniform-sized mesoporous materials and the sizes of CdS can be restricted. The smaller particle sizes facilitate the fast diffusion of charge carriers from the bulk of CdS to the surface active sites and this reduces the charge-carrier recombination. Second, the extremely large surface area of the support is conducive to the high dispersion of CdS species. Third, owing to the amorphous nature of the siliceous MCM-48 mesoporous support, the defects (oxygen vacancies) can serve as trap states. Thus, the pores neighboring the CdS species may provide an outlet for the holes generated in CdS to be trapped. This allows for the electrons to be localized on CdS to reduce protons and form hydrogen. Hence, the probability of electron–hole recombination is reduced. Fourth and most importantly, the host micro- or mesoporous materials minimize photocorrosion by encapsulating CdS species within their pores and partly limiting its exposure and contact with the aqueous electrolyte.

Cubic phased MCM-48 mesoporous materials are chosen as supports to accommodate the photoactive species. These materials possess large surface area, highly uniform mesoscale pores arrayed in a long-range periodicity and an inter-connected network of three-dimensional set of pores.[28] The pore geometry in MCM-48 facilitates enhanced diffusion of the reactant molecules compared to the uni-dimensional network of pores that are prevalent in MCM-41. Our recently published work reveals that the MCM-48 material, with its interconnected 3-D pore structure, facilitates good dispersion of titania when compared to the uni-dimensional pores that exist in MCM-41.[29] Thus, Ti-MCM-48 photocatalysts exhibit significantly enhanced apparent quantum efficiency for hydrogen production from water splitting compared to Ti-MCM-41 under identical experimental conditions. We have previously reported that cubic MCM-48 mesoporous materials can be used as a support to disperse and encapsulate CdS species. The CdS-MCM-48 materials show a relatively high apparent quantum yield (AQY) compared to CdS encapsulated in other micro- and mesoporous materials such as zeolite Y, ETS-4, ETS-10, and SBA-15.[27] Hence, in this work, we selected preformed Si-MCM-48 and Ti-MCM-48 (containing spatially isolated Ti^{4+} ions) mesoporous materials as host materials for dispersing CdS. Under visible light irradiation, the photoexcited electrons can migrate from the conduction band of CdS to the conduction band of TiO_2. The transfer of holes from the CdS valence band to that of TiO_2 is forbidden since the holes in the valence band of TiO_2 are at a more positive potential compared to CdS. Thus, charge-carrier recombination in CdS is minimized to some extent, and the photocatalytic efficiency of the CdS-Ti-MCM-48 based photocatalysts is increased compared to the bare CdS- and Ti-MCM-48 photocatalysts.

This is the *first* report to incorporate CdS and TiO_2 semiconductors into cubic phased MCM-48 mesoporous materials as a novel photocatalyst in which: (i) mild conditions for preparation of CdS–Ti–MCM-48 composites have been used, (ii) the band edges of photoactive species (CdS and TiO_2) dispersed on the mesoporous support have been calculated, (iii) visible light generation of H_2 in the absence of co-catalyst Pt which is usually indispensable for the production of hydrogen is realized, (iv) only *modest* photocorrosion ($<10\%$) of CdS is observed in the *absence* of sulfide or sulfite, (v) the life-time of the photogenerated electrons and the electron injection rate constants are calculated, (vi) evidence for transfer of electrons from CdS to TiO_2 is presented, (vii) a comprehensive characterization of the photocatalysts using a myriad of techniques (XRD, nitrogen isotherm, AAS, DRS, TEM, PL, time-resolved fluorescence, XPS, EPR, and UVPS) has been carried out, and importantly (viii) a relatively high apparent quantum efficiency (AQY) of 24.8% is realized.

2. Experimental

Pure siliceous MCM-48 (Si-MCM-48) and Ti-MCM-48 mesoporous materials were prepared by rapid and facile synthetic approaches at room temperature reported by us previously and more details are provided in the ESI† section.[30,31]

2.1. Synthesis of CdS-Si-MCM-48 and CdS-Ti-MCM-48 by a two-step modification method

0.15 g of Si-MCM-48 or Ti-MCM-48 was added to 50 mL of chloroform under vigorous stirring in a round bottom flask. After that, 1 mL of (3-mercaptopropyl) trimethoxysilane (MPTMS) was added to the suspension and the resulting suspension was stirred overnight at room temperature. Afterwards, the suspension was filtered and washed with chloroform and dichloromethane to

Table 1 Textural properties of all studied samples

Material	Si/CdS[a] (mol)	Si/CdS[b] (mol)	Surface area[c] ($m^2\ g^{-1}$)	Pore volume[d] ($cm^3\ g^{-1}$)	Pore diameter[e] (Å)
CdS-Si-MCM-48-MPTMS-25	25	42	943	0.59	17.2
CdS-Ti-MCM-48-01-MPTMS-5	5	17	915	0.58	17.0
CdS-Ti-MCM-48-01-MPTMS-25	25	36	743	0.47	17.0
CdS-Ti-MCM-48-01-MPTMS-50	50	79	986	0.61	17.0
CdS-Ti-MCM-48-21-MPTMS-5	5	22	855	0.53	17.0
CdS-Ti-MCM-48-21-MPTMS-25	25	33	823	0.46	16.9
CdS-Ti-MCM-48-21-MPTMS-50	50	77	897	0.57	17.0
CdS-Ti-MCM-48-31-MPTMS-25	25	35	1005	0.63	16.9

[a] Molar ratio in the gel. [b] Molar ratio in the product measured by AAS study. [c] Determined by applying the Brunauer–Emmett–Teller (BET) equation to a relative pressure (P/P_0) range of 0.05–0.30 to the adsorption isotherm. [d] Calculated from the amount of nitrogen adsorbed at the highest relative pressure (P/P_0) $\sim$ 0.98. [e] Calculated from the Barrett–Joyner–Halenda (BJH) equation using the desorption isotherm.

remove unreacted MPTMS. The wet paste was dried in an oven for 2 h at 80 °C. The dried sample was ground into a fine powder and added to 50 mL of methanol in a round bottom flask. A required amount of $Cd(OAc)_2{\cdot}2H_2O$ was added and the mixture was refluxed while being stirred at 70 °C for 24 h. Subsequently, the suspension was filtered and washed with hot methanol and dried at room temperature. Finally, treatment with H_2S at 70 °C for 6 h yielded the final product. The samples were named as CdS-Ti-MCM-48-MPTMS-X, where X represents the Si/CdS molar ratio in the synthesis gel. In this work, three different Si/CdS ratios were prepared. In total, 7 CdS–TiO_2 composites and 1 CdS based mesoporous photocatalyst were prepared and the final photocatalysts were named as CdS-Ti-MCM-48-01-MPTMS-50, CdS-Ti-MCM-48-01-MPTMS-25, CdS-Ti-MCM-48-01-MPTMS-5, CdS-Ti-MCM-48-21-MPTMS-50, CdS-Ti-MCM-48-21-MPTMS-25, CdS-Ti-MCM-48-21-MPTMS-5, CdS-Ti-MCM-48-31-MPTMS-25, and CdS-Si-MCM-48-MPTMS-25. The numbers (01, 21, and 31) after Ti-MCM-48 indicate the Si/Ti ratios of 200, 50, and 25 whereas the numbers (5, 25, and 50) after MPTMS indicate the Si/CdS ratios in the initial as-synthesized catalysts. Table 1 indicates the abbreviations used.

2.2. Structural characterization

Powder X-ray diffraction patterns (XRD) of the photocatalysts were recorded on a Rigaku Ultima IV X-ray diffractometer using Cu K_α radiation of λ = 1.540806 Å. N_2 adsorption–desorption isotherms of the photocatalysts were obtained on a Quantachrome Nova 2200*e* gas adsorption analyzer at 77 K. CdS content in the final CdS-Ti-MCM-48 materials was measured by using a Varian SpectrAA-200 atomic absorption spectrophotometer (AAS) equipped with a Cd cathode lamp. The transmission electron microscopy (TEM) image of a representative CdS-Ti-MCM-48 sample was obtained using a JEOL JEM-2100 LaB_6 TEM instrument equipped with the high-resolution style objective-lens pole piece at an acceleration voltage of 200 kV. UV-Vis diffuse reflectance spectra were acquired using a Cary 100 Bio UV-Visible spectrophotometer with praying mantis accessory (Harrick Scientific). A custom-designed Kratos Axis Ultra DLD X-ray photoelectron spectroscopy (XPS) system was used to investigate surface components of the CdS-Ti-MCM-48 materials. For the valence band determination study, UVPS scans were collected from the energy range 30 to −5 eV with 0.1 eV step size. The photoluminescence emission and excitation spectra were acquired on a Flouromax-4 fluorimeter (JY Horiba). Luminescence lifetimes of visible emission were acquired using a 0.46 M flat-field monochromator (Jobin-Yvon HR460), and a time-resolved photon-counting detection system consisting of a fast, red-sensitive, side-window photomultiplier. A digital oscilloscope (Tektronix, TDS 2022) was used. The pulsed excitation source for lifetime measurements was provided by an optical parametric oscillator (Opotek, Opolette). X-band continuous wave Electron paramagnetic resonance (EPR) experiments were conducted on a Bruker Elexsys E580 spectrometer equipped with an Oxford CF935 helium flow cryostat with an ITC-5025 temperature controller. More details regarding the experimental techniques are provided in the ESI† section.

2.3. Photocatalytic H_2 evolution

The photocatalytic activities of the samples were examined in a gas-closed system. A catalyst sample of 40 mg was dispersed in 10 mL of deionized water and 10 mL of ethanol in a 30 mL glass reactor. Prior to light irradiation, the photoreaction system was purged with high-purity argon for 30 min to remove air. The light source was a 300 W Xe lamp equipped with an optical cutoff filter (λ > 400 nm). The reaction proceeded under vigorous stirring using a magnetic stirring rod. The evolved H_2 gas was analyzed using gas chromatography SRI 8610C (molecular sieve column, TCD detector, argon as carrier gas).

3. Results and discussion

3.1. Powder XRD analysis

The room temperature synthesis of Si-MCM-48 and transition metal ion containing MCM-48 is usually a challenge. According to the synthetic methods developed by our group previously, titania containing MCM-48 mesoporous materials can be prepared at room temperature.[30] Furthermore, we have proven that the local coordination and environment of Ti^{4+} in the MCM-48 can be directed by prudently controlling the timing of the addition of the titanium precursor. Thus, the synthetic approach that leads to the most photoactive Ti-MCM-48 mesoporous materials, as described in the supplementary section, was employed in this work. The XRD patterns of Si-MCM-48 as well as Ti-MCM-48 samples indicate that the periodic arrangement of the cubic phased mesoporous structure was preserved.

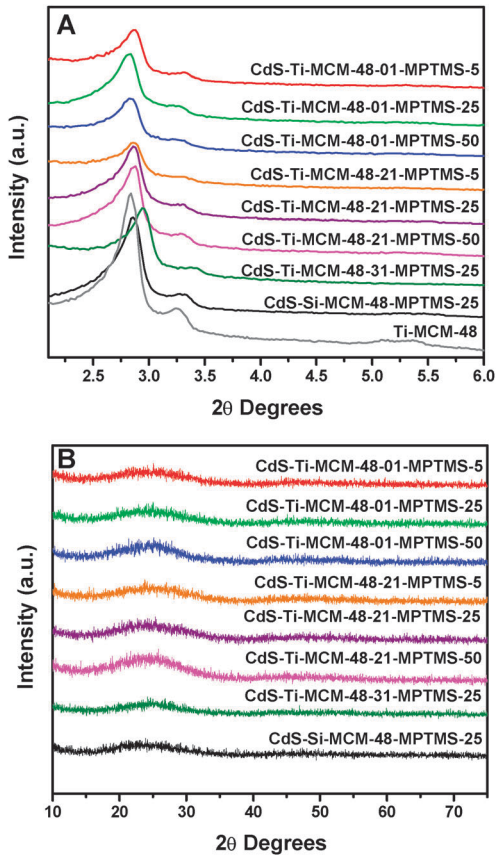

Fig. 1 (A) Low-angle and (B) high-angle XRD patterns of all studied samples.

Modification of the pore walls of Ti-MCM-48 mesoporous materials by (3-mercaptopropyl) trimethoxysilane makes the mesoscale porous structure of Si-MCM-48 and Ti-MCM-48 robust, thus enhancing the stability of the host mesoporous materials.[32,33] In addition, our previous work has demonstrated that $Cd(OAc)_2$, which is the cadmium(II) source in this work, is a mild and friendly cadmium(II) precursor for preparing a highly ordered cubic phase mesoporous MCM-48 containing well-dispersed CdS.[27]

In order to investigate the preservation of the cubic phased mesoscaled pores in CdS incorporated Si-MCM-48 and Ti-MCM-48 samples, powder X-ray diffraction (XRD) analysis was employed. Fig. 1A shows the low angle XRD patterns of the mesoporous samples. Clearly, all of the XRD patterns show typical Bragg reflections of the cubic phased MCM-48 mesoporous materials with cubic $Ia\bar{3}d$ symmetry. The strong peak near $2\theta = 3^\circ$ due to d_{211} reflections and the shoulder near $2\theta = 3.5^\circ$ due to d_{220} indicate that the three dimensional cubic phase of the pre-formed Si-MCM-48 as well as Ti-MCM-48 mesoporous materials were not affected by the loading of the CdS species.

The high angle XRD patterns of the samples are depicted in Fig. 1B. The plots exhibit only the characteristic peaks of amorphous SiO_2, which is the prevailing component of the MCM-48 mesoporous materials. The absence of the intrinsic XRD reflection peaks from TiO_2 and CdS indicate their high dispersion in the MCM-48 host. In addition, the reason for the lack of observation of peaks due to CdS and TiO_2 may also be due to the existence of very small (<3 nm) CdS and/or TiO_2 species consistent with our previous observations.

3.2. N_2 adsorption–desorption isotherms

Nitrogen physisorption study was carried out at 77 K to investigate the mesoporous structure of the composite photocatalysts. Fig. 2A shows the nitrogen adsorption isotherms of all the studied samples.

A typical, reversible type IV classification of isotherms is perceived in all studied samples indicating the mesoporous nature of these samples. Periodically arranged meso-scaled pores of CdS incorporated in Si-MCM-48 and Ti-MCM-48 samples adsorb N_2 (as monolayers) on the pore walls at low relative pressures ($P/P_0 < 0.1$). After the completion of monolayer adsorption, N_2 starts to form multilayers within the mesopores. A marked inflection is perceived between the relative pressures (P/P_0) = 0.1 and 0.2. This inflection, which is caused by capillary condensation, is an indication of the inherent mesoporosity present within the samples. The sharpness of the steep inflection has a strong correlation with the degree of the periodic arrangement of the mesopores. We notice that the sharpness of the inflections among all CdS containing samples exhibits

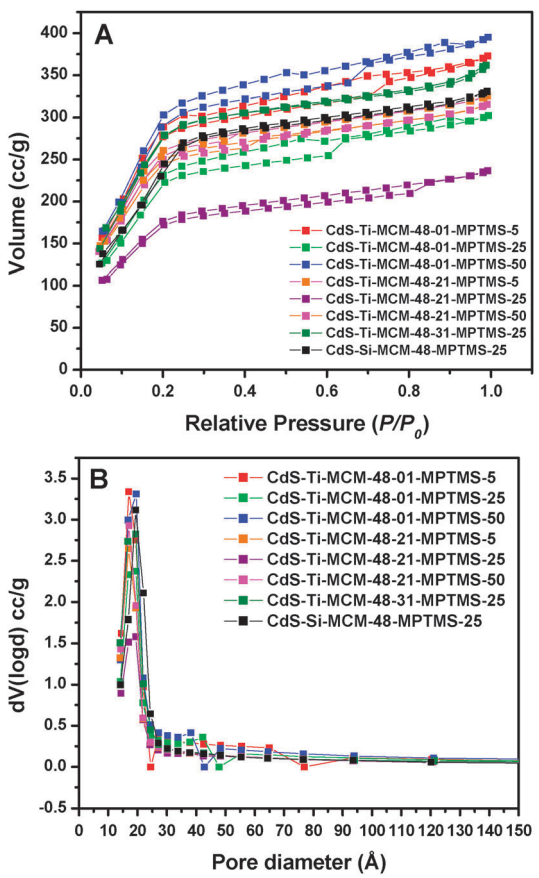

Fig. 2 (A) Nitrogen physisorption isotherms of all studied samples and (B) pore size distribution plots of all studied samples.

subtle variation with the different CdS contents. This observation illustrates that the CdS species can be well dispersed onto the MCM-48 mesoporous support and the MCM-48 host material displays periodic mesoporosity. The position of the inflection also provides an indication of the pore diameter. It can be seen that the position of the inflection remains relatively constant in CdS-Ti-MCM-48-MPTMS samples, indicating very little change in the pore diameter with change in the loading of CdS and TiO_2 species into the MCM-48 mesoporous materials.

Fig. 2B shows the pore size distribution of the samples prepared in this study. It can be seen that all of the studied samples show a highly uniform distribution of pore size. Moreover, there is little change in the pore size in the samples with different TiO_2 and/or CdS loadings, which demonstrates that CdS can be introduced into cubic Si-MCM-48 and Ti-MCM-48 mesoporous materials without sacrificing either the periodicity or the uniformity of the porous structure. In addition, it is noteworthy that compared to the as-synthesized Si-MCM-48 samples, reported in our previous studies, the (3-mercaptopropyl) trimethoxysilane (MPTMS) modified Si-MCM-48 and Ti-MCM-48 samples show shrinkage of pore size by only $\sim$2 nm. This is probably due to the rigidity of the MCM-48 porous structure upon modification by MPTMS. This observation has a pronounced effect on the reproducibility and universal applicability of our synthetic methods for preparing highly uniform and periodic CdS containing Si-MCM-48 and Ti-MCM-48 mesoporous photocatalysts.

A summary of the textural properties of all the studied samples is provided in Table 1. The Si/CdS molar ratios in the obtained samples were acquired by the atomic absorption spectrophotometric (AAS) study. A difference in the Si/CdS ratio in the synthesis gel and the final product can be noticed in all the samples. This apparent chemical loss can be explained by the elaborate washing procedures during the synthesis processes. Nonetheless, comparison of the Si/CdS ratio among the samples obtained by using the identical amounts of CdS precursors illustrates that the Si/CdS ratio remains nearly the same; for instance, in CdS-Si-MCM-48-MPTMS-25, CdS-Ti-MCM-48-01-MPTMS-25, CdS-Ti-MCM-48-21-MPTMS-25, and CdS-Ti-MCM-48-31-MPTMS-25 samples we can notice that the Si/CdS ratios in the final product and initial synthesis gel are fairly close, suggesting the good control of the CdS loading afforded by our synthetic method.

3.3. Transmission electron microscopy (TEM) and energy dispersive X-ray spectroscopy (EDS)

Transmission electron microscopy (TEM) and energy dispersive X-ray spectroscopy (EDS) were conducted to examine the periodic mesoporous nature of CdS-Ti-MCM-48 materials and the relative distributions of both CdS and TiO_2 species. Fig. 3A shows a representative TEM image of one sample, CdS-Ti-MCM-48-01-MPTMS-5, that contains high loading of CdS. The presence of a highly ordered arrayed mesoscaled porous structure can be perceived from the inset of Fig. 3A. This observation is in good agreement with the previously presented XRD and nitrogen physisorption results, in that the incorporation of CdS did not destroy the periodically arranged mesoporosities in the Ti-MCM-48 cubic phased mesoporous materials. In addition, it can be seen that the CdS species are fairly dispersed on the large surface area of the Ti-MCM-48 mesoporous host despite the fact that the loading of the CdS species is relatively high (Si/CdS = 17). The relative distributions of TiO_2 and CdS species were obtained from EDS studies. Fig. 3B presents the EDS spectra that reflect the chemical composition of the area represented by the black frame. The strong peaks due to Si and O, which represent MCM-48, can be found within this area. Meanwhile, a very weak peak from S is observed in Fig. 3B. This small S peak is likely caused by the unreacted MPTMS. The low intensity of the S peak indicates the presence of only a small amount of unreacted MPTMS. In contrast, the EDS spectra of the area that is enclosed by the white frame, shown in Fig. 3C, exhibit Cd and S peaks in addition to Si and O signals. Also, the C peak is strengthened and this is due to methylene groups in MPTMS. The Cu and part of the C peaks in both EDS plots are due to the use of carbon coated copper TEM grids. The EDS results strongly indicate that the dark spots are most likely ascribed to the formation of CdS species. Interestingly, no peaks due to Ti were detected from the EDS spectra. This may be due to the very small loading of titania in this sample (Si/Ti = 189). However, a clear peak due to Ti (not shown) can be noticed from the CdS-Ti-MCM-48-21-MPTMS-5 sample, in which the Si/Ti ratio is determined to be 22. Hence, the absence of the Ti peak in the CdS-Ti-MCM-48-01-MPTMS-5 sample is due to the extremely low amount of Ti loading and the high dispersion of these Ti nano species.

3.4. UV-Vis diffuse reflectance spectroscopy

UV-Vis diffuse reflectance spectroscopy (DRS) is a sensitive tool used to evaluate the size of CdS nanoparticles and the chemical environment of Ti^{4+} in MCM-48 host mesoporous materials. Fig. 4 shows the DRS spectra of CdS encapsulated in Si-MCM-48 and Ti-MCM-48 mesoporous materials. The bandgap of all materials in this study was calculated from the DRS spectra by extrapolating the high slope region to the *X*-axis. It is documented that a significant blue shift in the diffuse reflectance spectrum can be observed by anchoring semiconductor species to micro- or mesoporous host materials owing to the size quantization effect.[26,34,35] For the sake of unambiguous clarification and distinct visualization, the studied samples were divided into three groups according to either the host Ti-MCM-48 materials or the Si/CdS ratio in the samples and the results are shown in Fig. 4A–C respectively.

The onset of absorption of TiO_2 (due to Ti^{4+} ions in octahedral coordination) and CdS nanoclusters was calculated from the DRS spectra by extrapolating the respective high slope regions to the *X*-axis. As indicated in Fig. 4A–C, the absorption of titania may partially overlap with that of CdS even though the absorption onsets of titania and CdS are far apart. The absorption onsets of titania (due to Ti^{4+} ions in octahedral coordination) and CdS were determined to be near 325 nm and 445 nm as discussed in subsequent paragraphs.

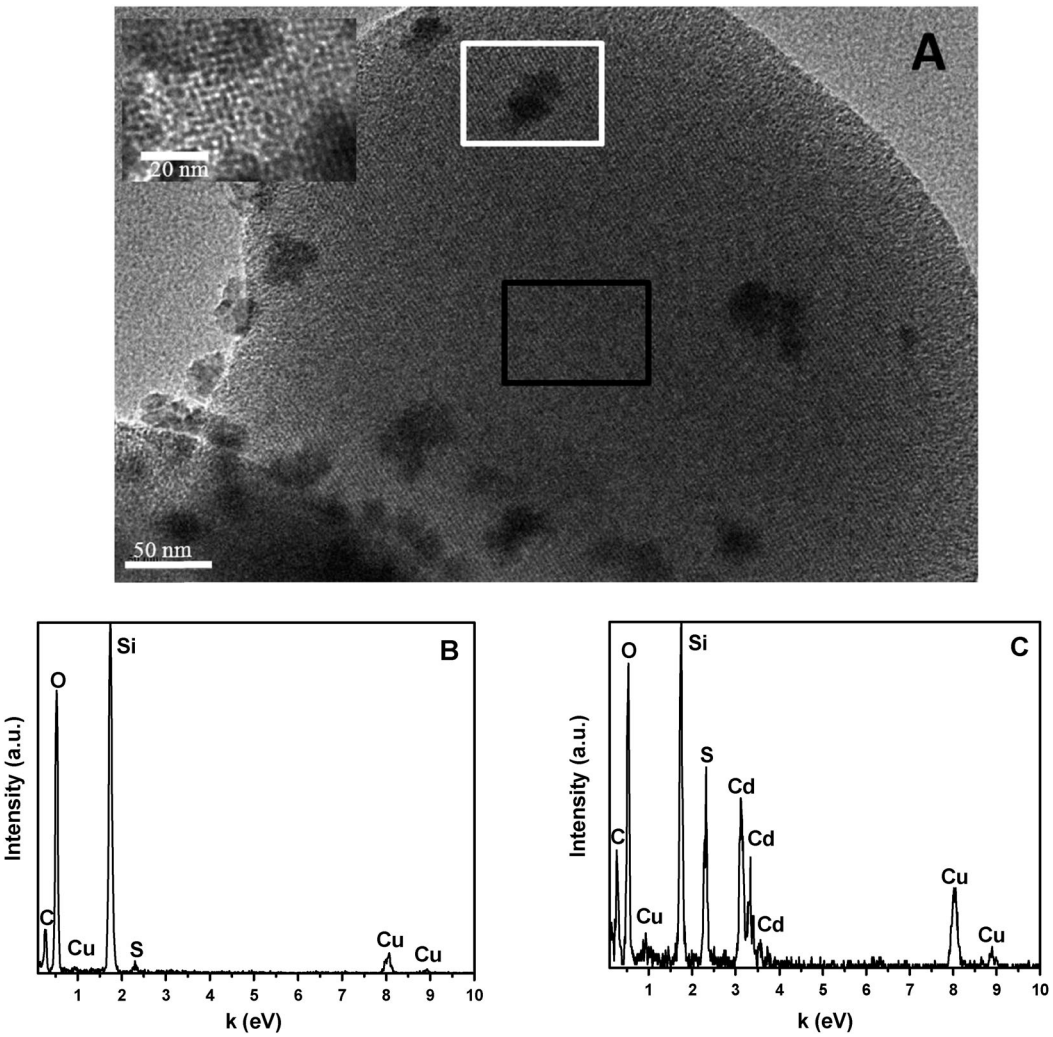

Fig. 3 (A) TEM image of CdS-Ti-MCM-48-01-MPTMS-5; (B) EDS plot of the black frame in (A); and (C) EDS plot of the white frame in (A).

In general, it can be seen in all figures that the absorption onset peak due to highly dispersed and/or spatially isolated TiO_2 nanoclusters in MCM-48 mesoporous materials varies from 320 to 325 nm and shows a remarkable blue shift compared to that of bulk TiO_2 (380 nm).

The band gaps of the TiO_2 species in these samples were determined to be in the range 3.82–3.87 eV. In Fig. 4A and B, a peak appearing at $\sim$210 nm in all the samples indicates a ligand-to-metal charge transfer (LMCT) from O^{2-} to Ti^{4+} ions in Ti-MCM-48 mesoporous host materials. This has been documented in the literature to be due to LMCT from O^{2-} to Ti^{4+} ions in tetrahedral coordination.[30] This suggests that the Ti^{4+} ions are incorporated into the silica framework of MCM-48 in Ti-MCM-48-01 and Ti-MCM-48-21 mesoporous materials, consistent with our previous observations.[29,30] Meanwhile, in Fig. 4A, a weak shoulder at $\sim$225 nm is seen in all of the Ti-MCM-48-01 samples, indicating that a small portion of Ti^{4+} is in distorted tetrahedral geometry. Compared to Ti-MCM-48-01, the DRS spectra of Ti-MCM-48-21 (Fig. 4B) also show a weak absorption band with a peak near $\sim$250 nm. This indicates that a fraction of Ti^{4+} in the Ti-MCM-48-21 samples is in the penta- or octahedral local environment due to the partial polymerization of Ti–O–Ti species as the titania amount increases.[36] However, the lack of absorption at $\sim$330 nm unambiguously rules out the presence of bulk TiO_2 in any of the Ti-MCM-48-01 and Ti-MCM-48-21 samples, which agrees with the results from the powder XRD studies, *i.e.* lack of detection of peaks due to bulk titania.

It is well known that Ti-MCM-48 mesoporous materials absorb only UV light. However, after the incorporation of CdS, the samples show an absorption band in the visible light region as seen in Fig. 4A–C. The absorption onset of bulk CdS occurs near 600 nm.[37] The absorption bands in CdS-Ti-MCM-48-01 and CdS-Ti-MCM-48-21 samples show onsets near 445 and 455 nm due to CdS. The bandgap of CdS species in these samples is estimated to be 2.78 eV and 2.73 eV respectively. The remarkable blue shift in the absorption spectrum is due to the quantum size effect, which indicates that the CdS particles are confined primarily in the mesopores of Ti-MCM-48. The particle size of the CdS species in these two mesoporous MCM-48 materials was determined to be in the range of 2.6 to 2.9 nm by applying the Brus equation.[38,39] Also, the absorption band remains almost constant in each set of the samples

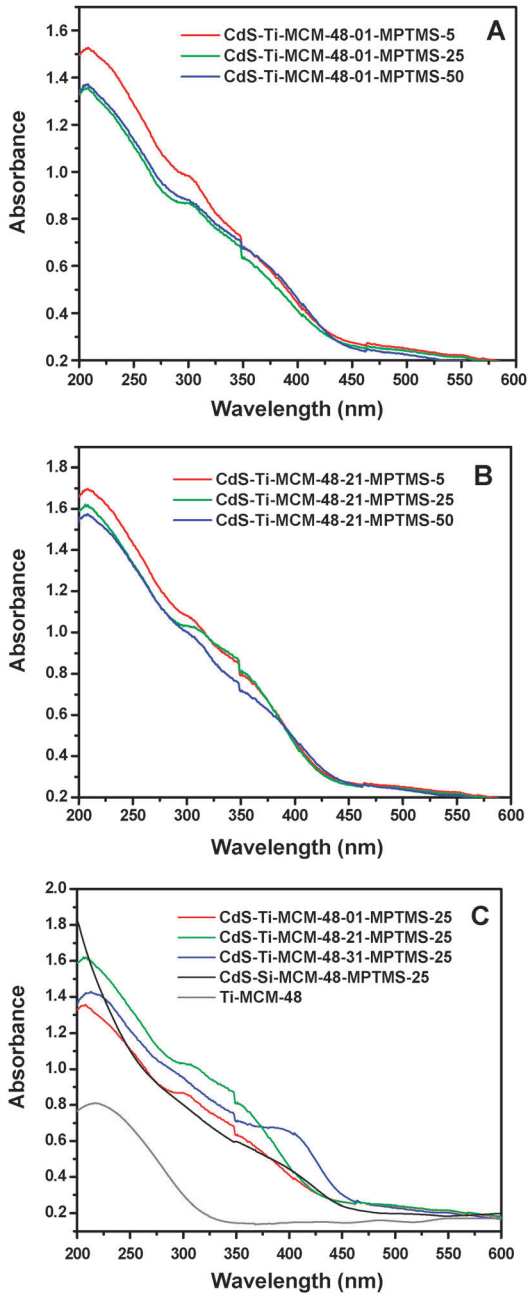

Fig. 4 (A) Diffuse reflectance spectra of CdS incorporated in Ti-MCM-48-01 series of samples; (B) diffuse reflectance spectra of CdS incorporated in Ti-MCM-48-21 series of samples; and (C) comparative diffuse reflectance spectra of CdS incorporated in host Si- and Ti-MCM-48 materials.

as shown in Fig. 4A and B. This observation again illustrates the high dispersion of CdS species into the Ti-MCM-48 mesoporous host. However, the particle size of CdS determined from the Brus equation is greater than the pore size of Ti-MCM-48 mesoporous materials. This is caused by the quantum tunneling effect and is commonly seen in CdS embedded in micro- and mesoporous materials.[27,40] Through this process, CdS species agglomerate through the fairly open 3-D inter-penetrating network of the cubic phased Ti-MCM-48 host materials to form larger particles.

Our nitrogen adsorption studies clearly indicate that most of the CdS particles are located inside the pores of MCM-48. However, we cannot completely rule out the possibility of small amounts CdS particles that are deposited on the surface of the material despite extensive washing. Thus, there could be very small amounts of CdS particles that are not deposited within the pores of the MCM-48 mesoporous material.

Fig. 4C shows the DRS spectra of CdS incorporated into various cubic phased mesoporous host materials. In comparison to Ti-MCM-48-01 and Ti-MCM-48-21, Ti-MCM-48-31 possesses an absorption band centered at $\sim$220 nm that indicates a fraction of Ti^{4+} is in distorted tetrahedral geometry. The formation of such coordination of Ti^{4+} can be ascribed to the aggregation of titania species in the mesoporous materials at relatively high titania loading as in this sample. However, the bulk form of TiO_2 can be ruled out from the absence of an absorption peak at $\sim$330 nm. In addition, the absorption onsets due to CdS in CdS-Si-MCM-48-MPTMS-25, CdS-Ti-MCM-48-01-MPTMS-25, and CdS-Ti-MCM-48-21-MPTMS-25 are similar.

However, in CdS-Ti-MCM-48-31-MPTMS-25, an apparent red shift of the absorption onset occurs, which suggests that larger CdS particle sizes of $\sim$3 nm are formed in this sample. The bandgap energies of TiO_2 and CdS species are calculated to be 3.76 eV and 2.64 eV respectively in this sample.

3.5. XPS and UVPS analysis

Our XPS studies indicate that CdS-Ti-MCM-48 samples (Si/CdS = 5 with varying Si/Ti ratios of 200 (CdS-Ti-MCM-48-01-MPTMS-5) and 50 (CdS-Ti-MCM-48-21-MPTMS-5)) show relatively high intensities due to Cd in comparison to Ti and hence there is significant uncertainty in estimating the valence band edge positions in these 2 samples and hence these set of samples were not investigated for UVPS studies. Similarly, CdS-Ti-MCM-48 samples (Si/CdS = 50 with varying Si/Ti ratios of 200 (CdS-Ti-MCM-48-01-MPTMS-50) and 50 (CdS-Ti-MCM-48-21-MPTMS-50)) show relatively low signals due to Cd^{2+} ions and hence these set of samples were also not used for UVPS studies. Thus, only CdS-Ti-MCM-48 samples (Si/CdS = 25 with varying Si/Ti ratios of 200 (CdS-Ti-MCM-48-01-MPTMS-25), 50 (CdS-Ti-MCM-48-21-MPTMS-25), and 25 (CdS-Ti-MCM-48-31-MPTMS-25)) were studied for UVPS analysis in this work. The XPS scan of one representative CdS-Ti-MCM-48-31-MPTMS material is shown in Fig. 5. The peak at 532.6 eV is attributed to the Si–O bond. Furthermore, a small peak at 530.3 eV is obtained indicating the presence of the Ti–O bond. The high resolution XPS spectrum of the Ti 2p region in Fig. 5B shows split peaks ($2p_{3/2}$ and $2p_{1/2}$) at 458.7 and 464.4 eV. The peak separation between Ti $2p_{3/2}$ and $2p_{1/2}$ is 5.7 eV fitting with the standard binding energy of Ti^{4+} species. The Cd $3d_{5/2}$ and $3d_{3/2}$ peaks at 404.9 and 411.6 eV corresponding to the Cd^{2+} species are shown in Fig. 5C. The split energy of 6.7 eV between Cd $3d_{5/2}$ and $3d_{3/2}$ peaks suggests the formation of CdS. Similarly, two S 2p peaks at 161.3 and 162.5 eV in Fig. 5D are also observed. These peaks are attributed to the S^{2-} of CdS. Moreover, two more peaks at 163.2 and 164.4 eV due to free thiol species are observed. In order to estimate the valence band edges of CdS and TiO_2 in CdS-Ti-MCM-48 materials, ultraviolet

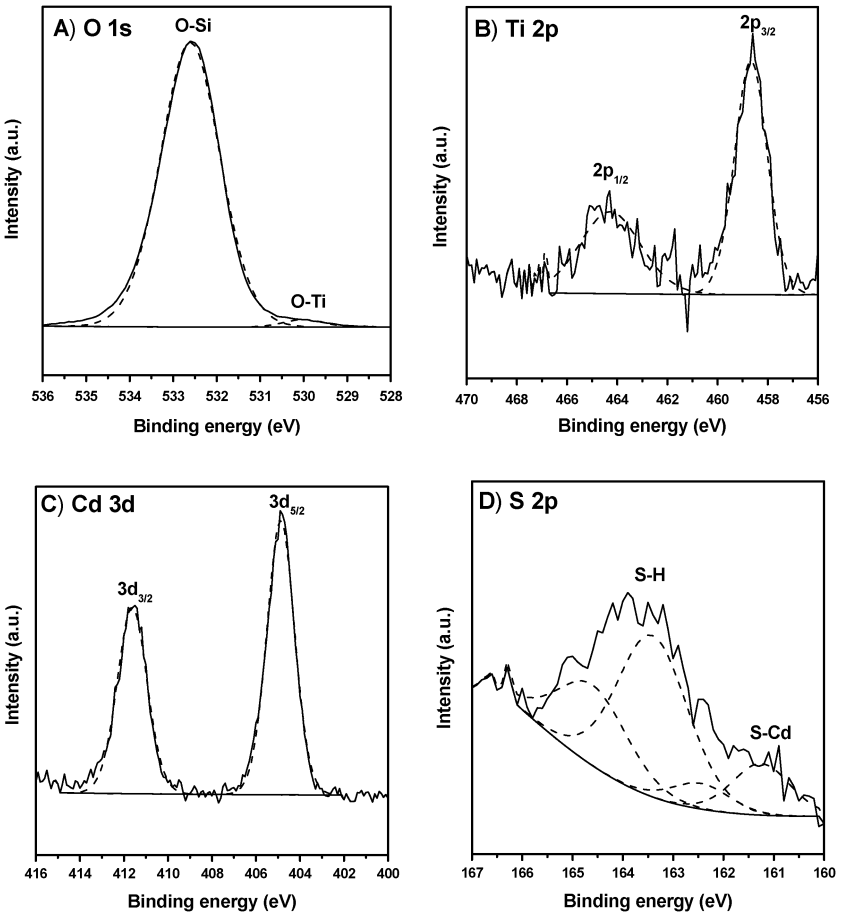

Fig. 5 (A) XPS of O peaks from the CdS-Ti-MCM-48-31-MPTMS-25 sample; (B) XPS of Ti peaks from the CdS-Ti-MCM-48-31-MPTMS-25 sample; (C) XPS of Cd peaks from the CdS-Ti-MCM-48-31-MPTMS-25 sample; and (D) XPS of S peaks from the CdS-Ti-MCM-48-31-MPTMS-25 sample.

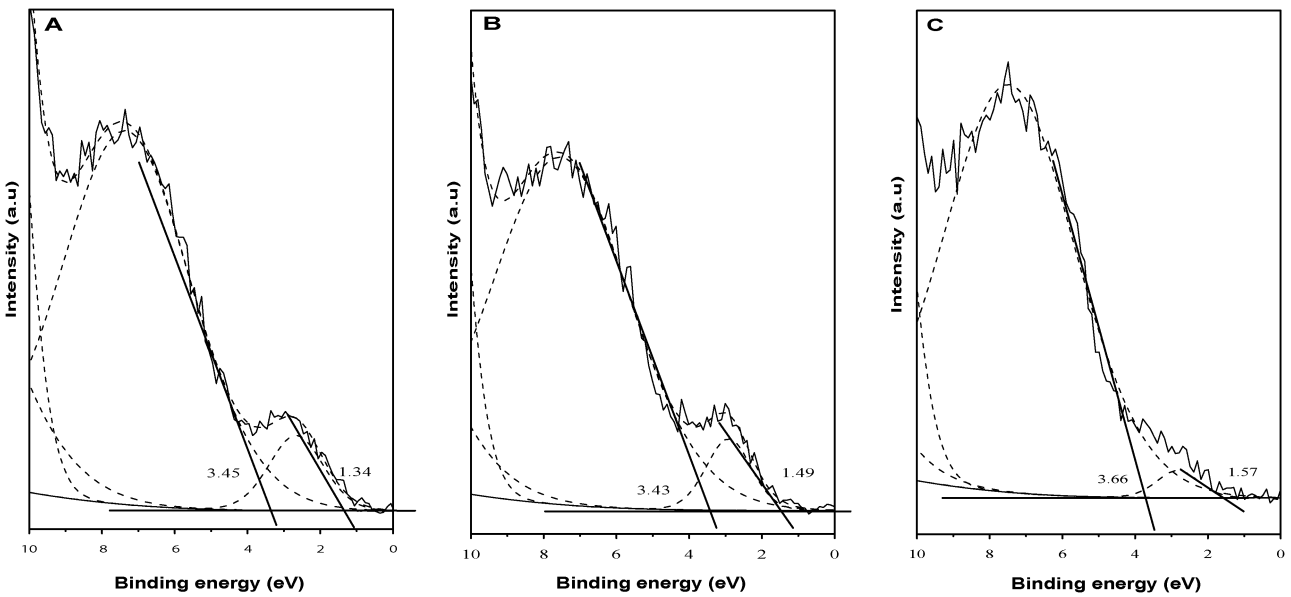

Fig. 6 UVPS of (A) CdS-Ti-MCM-48-01-MPTMS-25; (B) CdS-Ti-MCM-48-21-MPTMS-25; and (C) CdS-Ti-MCM-48-31-MPTMS-25 samples with estimation of TiO_2 and CdS valence band edge positions.

Table 2 Summary of the conduction and valence band edge of CdS and TiO_2 with reference to the normal hydrogen electrode (NHE) in the studied samples

Photocatalyst	CdS bandgap energy (eV)	TiO_2 bandgap energy (eV)	CdS valence band edge (eV)	CdS conduction band edge (eV)	TiO_2 valence band edge (eV)	TiO_2 conduction band edge (eV)
CdS-Ti-MCM-48-01-MPTMS-25	2.78	3.87	1.34	−1.44	3.45	−0.42
CdS-Ti-MCM-48-21-MPTMS-25	2.73	3.82	1.49	−1.24	3.43	−0.39
CdS-Ti-MCM-48-31-MPTMS-25	2.64	3.76	1.57	−1.07	3.66	−0.10

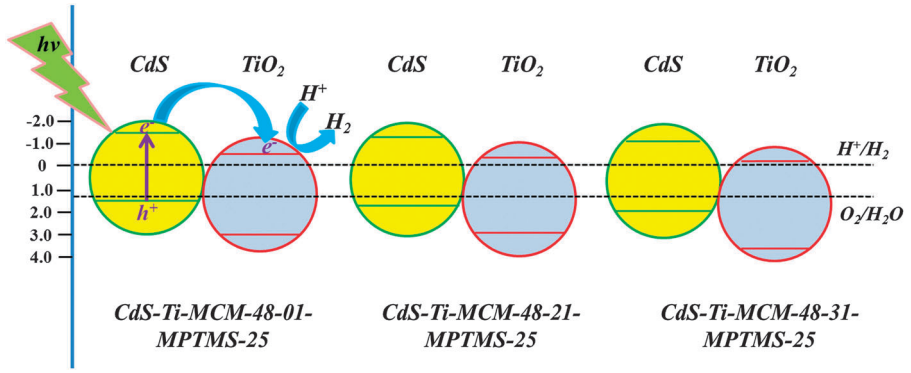

Scheme 1 Conduction and valence band diagram of CdS incorporated Ti-MCM-48 samples.

photoelectron spectroscopy (UVPS) scan was employed. Fig. 6 shows UVPS spectra of CdS-Ti-MCM-48-01-MPTMS-25, CdS-Ti-MCM-48-21-MPTMS-25, and CdS-Ti-MCM-48-31-MPTMS-25 samples. For measurement, two simulated peaks with peak centers at 7.5 and 2.8 eV are established. Consequently, the valence band maximum (VBM) of 3.66 and 1.57 eV is measured for TiO_2 and CdS respectively, based on previous reports.[41,42] Combining the bandgap energy determined from the DRS studies and the information regarding the valence band edges from UVPS studies, the band edge positions of both the conduction and valence bands of CdS and TiO_2 in these composite photocatalysts can be obtained. The values of the band edge positions of the studied samples are listed in Table 2.

According to the band edge values obtained from the DRS and UVPS studies, a schematic representation of the band structures of CdS and TiO_2 in the studied samples is depicted in Scheme 1. It can be seen that in all studied CdS-Ti-MCM-48-MPTMS samples, the conduction band of CdS is residing at a more negative value than that of TiO_2. Hence, the photoexcited electrons on the CdS conduction band can diffuse to the TiO_2 conduction band. This process is conducive to the effective charge separation and facilitates the improvement of photocatalytic efficiency of photogenerated charge carriers. Also, the TiO_2 conduction band is located at a more negative value than the H^+/H_2 redox potentials in all studied samples. Furthermore, the conduction band edge of TiO_2 shifts to more positive values with increase in titania amounts.

3.6. Solar hydrogen evolution from photocatalytic water splitting

The photocatalytic activity of the CdS-Si-MCM-48 and CdS-Ti-MCM-48 samples upon water splitting was studied under visible light illumination, and the yields of solar hydrogen were determined by gas chromatography. Fig. 7 shows the solar hydrogen evolution rate from all of the samples under identical experimental conditions. In general, all of the samples exhibit photocatalytic activity over water splitting from the irradiation of visible light with the presence of ethanol as a sacrificial reagent. Fig. 7A presents the photocatalytic activity of the samples based on Ti-MCM-48-01 mesoporous host materials. It can be seen that, in this series of samples, the hydrogen evolution rate increases with the loading of CdS. This trend is also maintained in the Ti-MCM-48-21 supported CdS containing set of samples shown in Fig. 7B. Clearly, the photocatalytic hydrogen evolution rate is enhanced along with an increase in the amount of CdS in the photocatalyst.

In addition to the effect of CdS content on the photocatalytic activity, the TiO_2 content was also varied. Fig. 7C shows a plot of the photocatalytic hydrogen evolution rate with varying titania contents. It can be seen that the amount of the TiO_2 component plays a positive role in the photocatalytic reaction, which is indicated by an increase in solar hydrogen productivity from CdS-Si-MCM-48-MPTMS-25 to CdS-Ti-MCM-48-31-MPTMS-25.

Table 3 shows the photocatalytic hydrogen evolution rate of all studied samples along with their corresponding apparent quantum yield (AQY). A more detailed discussion of the role of CdS and TiO_2 in the coupled semiconductor incorporated mesoporous photocatalysts can be made by combining the photocatalytic activity and fluorescence emission decay studies as shown in the next section.

3.7. Photoluminescence and time-resolved fluorescence emission decay studies

To be better informed of the photogenerated charge transfer pathways and the photocatalytic reaction mechanisms in the binary semiconductor containing a mesoporous materials

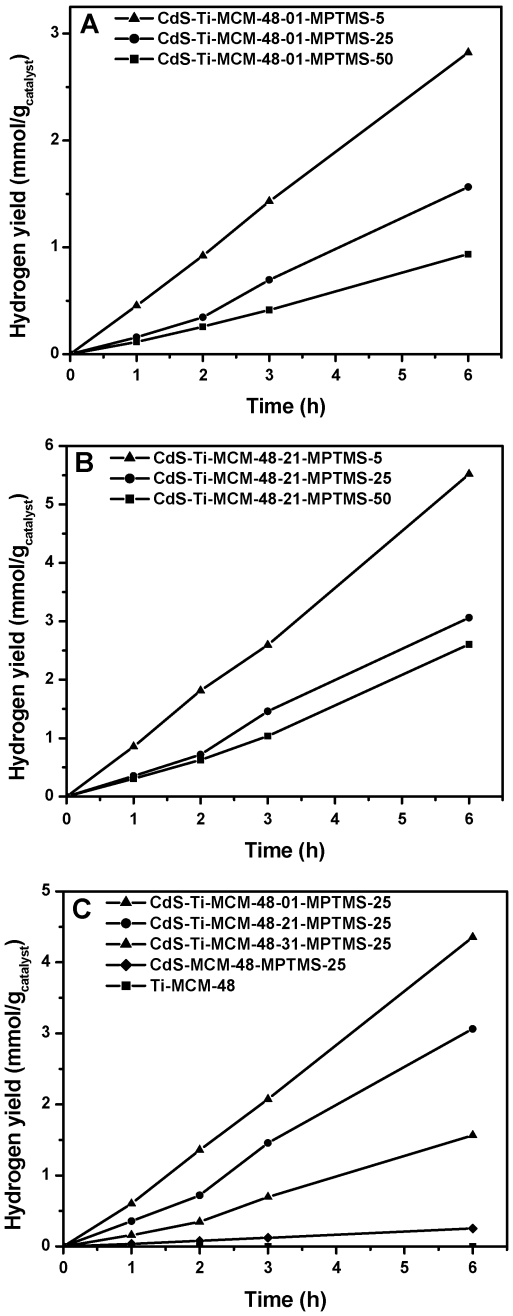

Fig. 7 Photocatalytic hydrogen production as a function of reaction time for (A) CdS-Ti-MCM-48-01 series samples; (B) CdS-Ti-MCM-48-21 series samples; and (C) samples with Si/CdS = 25 molar ratios from different Ti-MCM-48 samples.

supported system, time-resolved fluorescence emission decay studies were carried out. Fig. 8 shows the emission spectrum of CdS-Ti-MCM-48-01-MPTMS-25 under excitation at 397 nm. The emission spectrum shows a broad band centered at 600 nm. Since there is no luminescence observed in the Si-MCM-48 sample, the emission at 600 nm can be ascribed to the existence of the CdS species. When CdS is coupled to Ti-MCM-48, a significant quenching of the emission is observed compared to CdS-Si-MCM-48. Since the conduction band of Ti-MCM-48 lies

Table 3 Summary of the photocatalytic hydrogen evolution rate and the apparent quantum yield (AQY) of the studied samples

Photocatalyst	Hydrogen evolution rate (mmol h^{-1} $g_{catalyst}^{-1}$)	Apparent quantum yield[a] (AQY) (%)
CdS-Si-MCM-48-MPTMS-25	0.042	1.1
CdS-Ti-MCM-48-01-MPTMS-50	0.156	4.2
CdS-Ti-MCM-48-01-MPTMS-25	0.261	7.0
CdS-Ti-MCM-48-01-MPTMS-5	0.470	12.7
CdS-Ti-MCM-48-21-MPTMS-50	0.434	11.7
CdS-Ti-MCM-48-21-MPTMS-25	0.511	13.8
CdS-Ti-MCM-48-21-MPTMS-5	0.920	24.8
CdS-Ti-MCM-48-31-MPTMS-25	0.726	19.6

[a] $\mathrm{AQY}(\%) = \dfrac{\text{the number of evolved } H_2 \text{ molecules} \times 2}{\text{the number of incident photons}} \times 100$

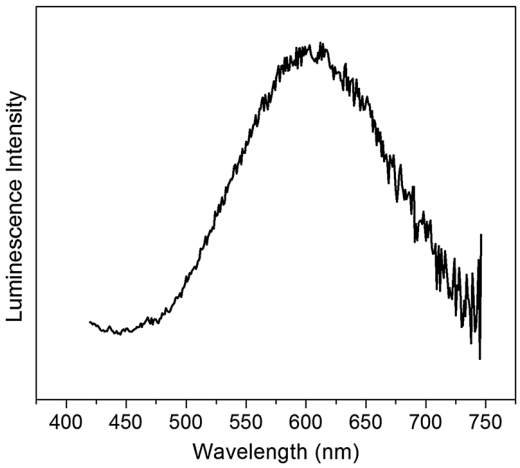

Fig. 8 Emission spectrum of CdS-Ti-MCM-48-01-MPTMS-25 under excitation at 397 nm. The emission spectrum shows a broad band centered at 600 nm.

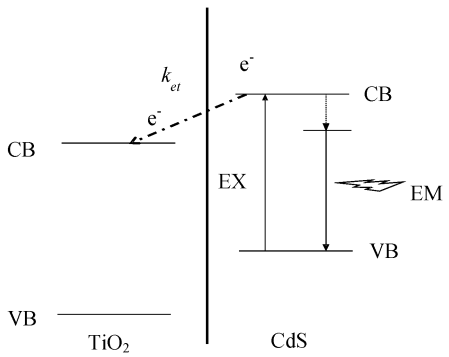

Scheme 2 Luminescence mechanism in the CdS-Ti-MCM-48 sample. CB, VB, EX, and EM refer to the conduction band, valence band, excitation and emission.

at a less negative value than the CdS conduction band, electron injection is expected from the photoexcited CdS species into TiO_2.

Therefore, after photo-excitation of the CdS species in Ti-MCM-48 samples, the electrons generated relax *via* two pathways: (1) trapping into deep trap (DT) states and further

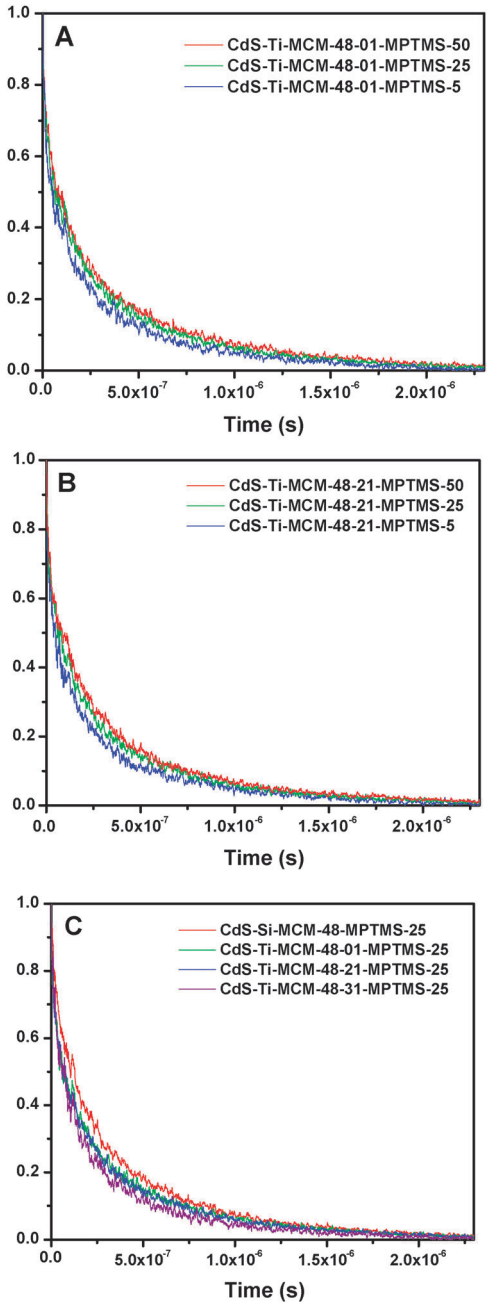

Fig. 9 Normalized, decay curves of (A) CdS-Ti-MCM-48-01 series; (B) CdS-Ti-MCM-48-21 series; and (C) samples with Si/CdS = 25 molar ratios from different preformed Ti-MCM-48 samples by monitoring 580 nm emission under excitation at 440 nm.

recombination with holes in the valence band and/or (2) injection into the conduction band of TiO_2, as shown in Scheme 2.

Fig. 9 shows the decay curves of the mesoporous photocatalysts by monitoring the 580 nm emission from CdS. All the samples were excited at 440 nm to ensure that electrons can only be excited from the CdS valence band, since TiO_2 does not have any absorption onset at a wavelength of 440 nm according to the diffuse reflectance spectra in Fig. 4. The luminescence lifetimes (τ) and the electron transfer rate constant (k_{et}) were calculated using the following equations:

$$\tau = \int_0^\infty \varphi(t)\mathrm{d}t \quad (1)$$

$$k_{et} = \frac{1}{\tau} \quad (2)$$

where $\varphi(t)$ is the luminescent decay curve normalized such that $\varphi(0) = 1$. The definition of lifetime given by eqn (1) is useful because: (1) it is not model dependent and (2) it can be used to relate to the relative quantum efficiency of donor luminescence in the presence and absence of acceptors as described previously by Inokuti and Hirayama[43,44]

$$q/q_0 = \tau/\tau_0 \quad (3)$$

where q_0 and τ_0 are the quantum efficiency and lifetime, respectively, of the donor in the absence of acceptors. The calculated lifetimes are listed in Table 4.

From Fig. 9A, B and Table 4, we can infer that the lifetime of the electron residing in CdS decreases with an increase in the loading of CdS. A high loading of CdS leads to a higher chance of contact between CdS and TiO_2 species. Since the conduction band of TiO_2 is located at a less negative potential than that of CdS, the electrons can be injected from the conduction band of CdS to the conduction band of TiO_2.[45–47] The extra pathway provided for electrons from the conduction band of CdS to the conduction band of TiO_2 increases the electron transfer rate constant (k_{et}), and hence, the lifetime of electrons on the CdS conduction band is shortened.[48,49] This decrease in the lifetime of electrons on the CdS conduction band can also be correlated with the photocatalytic activity. As stated previously, the photocatalytic hydrogen evolution rate increases with an increase in the CdS amount in the photocatalysts. An enhancement of the photocatalytic activity can be rationalized by the fast transfer of electrons from the CdS conduction band to the TiO_2 conduction band. This process dramatically reduces the charge-carrier recombination in CdS. Hence, the photoexcited electrons can be effectively harnessed for the photocatalytic reaction to produce hydrogen.

In addition, we also studied the lifetimes of the electrons on CdS as a function of TiO_2 amount. Fig. 9C shows the decay curves of a series of CdS-Ti-MCM-48 samples containing different Ti loadings. The lifetimes of the samples decrease as the amounts of TiO_2 loadings increase. This observation can be again explained by the fast transfer of electrons from the CdS conduction band to the TiO_2 conduction band.[50] With an increase in the TiO_2 component, more intimate contact between CdS and TiO_2 can be obtained. The larger the amount of TiO_2 in contact with the CdS species, the larger is the number of paths for the photoexcited electrons in the CdS conduction band to dissipate their charge; thus, the lifetime of the electrons on the CdS conduction band is curtailed. Taking the photocatalytic activity of these samples into account, a shorter lifetime of electrons in the CdS conduction band can be seen in the samples that possess higher photocatalytic activity.

Table 4 Fluorescence lifetimes, electron injection rate constants as well as the hydrogen evolution rate of the studied samples

Sample λ_{em} = 580 nm	τ (ns)	k_{et} (10^6 s^{-1})	η_{et} (%)	Hydrogen evolution rate (mmol h^{-1} $g_{catalyst}^{-1}$) and AQY
CdS-Si-MCM-48-MPTMS-25	292.7	0	0	0.042 (1.1%)
CdS-Ti-MCM-48-01-MPTMS-50	271.3	0.27	7.3	0.156 (4.2%)
CdS-Ti-MCM-48-01-MPTMS-25	245.9	0.65	16.0	0.261 (7.0%)
CdS-Ti-MCM-48-01-MPTMS-5	204.3	1.47	30.0	0.470 (12.7%)
CdS-Ti-MCM-48-21-MPTMS-50	263.0	0.38	10.0	0.434 (11.7%)
CdS-Ti-MCM-48-21-MPTMS-25	238.1	0.78	18.6	0.511 (13.8%)
CdS-Ti-MCM-48-21-MPTMS-5	197.9	1.63	33.3	0.920 (24.8%)
CdS-Ti-MCM-48-31-MPTMS-25	205.3	1.45	30.0	0.726 (19.6%)

Once the electron transfer rate constant of the CdS species in Si-MCM-48 ($k_{(CdS\text{-}MCM\text{-}48)}$) is known from the decay curve of the CdS-MCM-48 sample, one can calculate the rate constant for the electron injection to TiO_2 by subtracting the rate constant of CdS species in Si-MCM-48 ($k_{(CdS\text{-}MCM\text{-}48)}$) from the rate constant obtained from the CdS-Ti-MCM-48 samples ($k_{(CdS\text{-}Ti\text{-}MCM\text{-}48)}$), as shown in eqn (4). The electron injection rate constant k_{et} can then be expressed by:

$$k_{et} = k_{(CdS\text{-}Ti\text{-}MCM\text{-}48)} - k_{(CdS\text{-}MCM\text{-}48)} = \frac{1}{\tau_{(CdS\text{-}Ti\text{-}MCM\text{-}48)}} - \frac{1}{\tau_{(CdS\text{-}MCM\text{-}48)}} \quad (4)$$

where $k_{(CdS\text{-}Ti\text{-}MCM\text{-}48)}$ and $\tau_{(CdS\text{-}Ti\text{-}MCM\text{-}48)}$ represent the rate constant and the lifetime of the electron in the conduction band of CdS species encapsulated inTi-MCM-48 respectively; $k_{(CdS\text{-}MCM\text{-}48)}$ and $\tau_{(CdS\text{-}MCM\text{-}48)}$ represent the rate constant and lifetime of electrons in the conduction band of CdS in Si-MCM-48 respectively. Based on the calculated k_{et}, it is easy to calculate the electron injection efficiency η_{et} by using eqn (5), and the calculated results are listed in Table 4.

$$\eta_{et} = k_{et}/k_{(Cds\text{-}Ti\text{-}MCM\text{-}48)} \quad (5)$$

A plot of the AQY as a function of the electron injection efficiency (η_{et}) is shown in Fig. S1 (ESI†). In general, it can be seen that AQY increases with η_{et}. In the sample, CdS-Ti-MCM-48-21-MPTMS-5, which possesses the highest photocatalytic hydrogen evolution rate, the most efficient electron injection from CdS to TiO_2 can be achieved. However, exceptions can also be observed in two of the samples (CdS-Ti-MCM-48-01-MPTMS-5 and CdS-Ti-MCM-48-21-MPTMS-50), in which the electron injection efficiency does not exactly mirror the AQY. The discrepancies between AQY and η_{et} in these two samples may be ascribed to differences in MPTMS loadings and silanol defects in these 2 samples in comparison to the rest of the 6 samples that result in small deviations in the calculated electron injection rate from CdS to TiO_2.

3.8. Electron paramagnetic resonance (EPR)

In order to verify and identify the fate of the photogenerated electrons from CdS species, electron paramagnetic resonance (EPR) spectroscopic studies were carried out. EPR spectra reveal the presence of Ti^{3+} after irradiation by visible light (>400 nm) confirming that the photogenerated electrons from the CdS conduction band are successfully injected into TiO_2 (Fig. S2, ESI†). The signals with $g_\perp$ = 1.966 and $g_\parallel$ = 1.913 that can be perceived in Fig. S2 (ESI†) are the evidence for the presence of Ti^{3+} in CdS-Ti-MCM-48-31-MPTMS-25.[29,51,52] In addition to the signals that are due to the presence of Ti^{3+}, an axially asymmetric signal with g_x = 2.063, g_y = 2.027, and g_z = 2.000 was observed, which corresponds to the disulfide radicals ($RSS^\bullet$) that were generated from the oxidation of MPTMS species in the sample.[53] Combining with the results from time-resolved fluorescence emission decay studies and EPR analysis, a conclusion can be made that coupling CdS with TiO_2 realizes efficient photoinduced electron transfer from CdS to TiO_2 so that the photocatalytic activity is enhanced and charge carrier recombination is minimized.

3.9. Recycling studies

To examine the reproducibility of solar hydrogen yields generated by CdS-Ti-MCM-48 samples, recycling studies were carried out. Fig. 10 shows the photocatalytic hydrogen yield of three different photocatalysts after irradiation for 18 h; all of the values are listed in Table S1 (ESI†). It can be clearly perceived that the hydrogen evolution rate in all the samples remains almost constant after a long period of irradiation, *even* without using either sulfide and/or sulfite salts or precious metal Pt as a co-catalyst. The highly reproducible hydrogen evolution yields

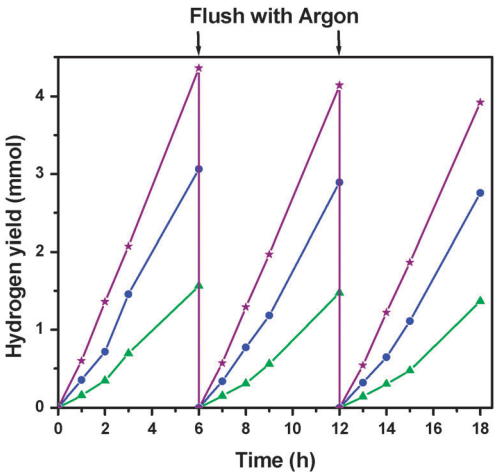

Fig. 10 Photocatalytic hydrogen evolution over (★) CdS-Ti-MCM-48-31-MPTMS-25, (●) CdS-Ti-MCM-48-21-MPTMS-25, and (▲) CdS-Ti-MCM-48-01-MPTMS-25 samples and their spent catalysts.

indicate that CdS–TiO_2 coupled semiconductor incorporated MCM-48 supported mesoporous materials are quite robust and show sustained production of hydrogen in the presence of visible light.

To be better informed about the structure of the spent catalysts, the photocatalysts were carefully collected after the reactions and characterized by several techniques. Fig. S3 (ESI†) shows the low angle powder XRD patterns of a representative fresh and spent CdS-Ti-MCM-48 sample. It can be seen (Fig. S3A, ESI†) that the cubic phase, which is evident in the typical Bragg reflections with cubic $Ia\bar{3}d$ symmetry of the MCM-48 mesoporous support materials, along with the highly periodic arrangement of mesoscale pores, was preserved even after 18 h of irradiation by visible light under our experimental conditions. Meanwhile, the high angle XRD patterns of these two samples depicted in Fig. S3B (ESI†) exhibit characteristic peaks of bulk SiO_2. The powder XRD results suggest that the CdS–TiO_2 coupled semiconductors incorporated in the cubic phased MCM-48 mesoporous materials supported novel photocatalysts are fairly stable under visible light irradiation. The CdS and TiO_2 species remain widely dispersed even after long periods of irradiation.

Fig. S4A (ESI†) shows the nitrogen adsorption–desorption isotherms of CdS-Ti-MCM-48-31-MPTMS-25 sample and its spent product. Both isotherms are of typical type IV classification, which is proof of the mesoporous nature of both the samples. In addition, the similar position of sharp inflection, which correlates with the pore sizes in mesoporous materials, observed in both isotherms indicates no change in the pore diameter of the host MCM-48 mesoporous materials after the photocatalytic reaction. This can be seen from the pore size distribution plots of the two studied samples as shown in Fig. S4B (ESI†). In general, nitrogen physisorption studies are in good agreement with powder XRD analyses. Both of them suggest that the highly ordered cubic phased mesoporous structures of the photocatalysts are not diminished after the photocatalytic processes and that both CdS and TiO_2 are widely dispersed in the host mesoporous material. A summary of the textural properties of the studied fresh and spent catalysts is provided in Table S2 (ESI†). The XPS study of a representative spent catalyst, CdS-Ti-MCM-48-31-MPTMS-25-spent, was also performed. The XPS results for the Cd 3d core level exhibit doublet peaks at $3d_{3/2}$ 411.6 eV and $3d_{5/2}$ 404.9 eV ascribed to CdS based materials. Moreover, the S $2p_{1/2}$ and S $2p_{3/2}$ peaks appear at 162.4 eV and 161.2 eV supporting the retention of CdS. The ratio of peak areas of Cd and S peaks was found to be similar before and after the photocatalytic reaction. This result suggests that no change occurred in the chemical state of CdS after the water splitting reaction. Moreover, the AAS study of the spent catalyst suggests a similar Si/CdS ratio compared to that in the fresh one. This result indicates that only a very small amount of CdS is lost after the photocatalytic reaction. Therefore, the spent catalysts maintain almost the same photocatalytic activities as compared to the fresh ones.

4. Conclusions

CdS was incorporated into Si-MCM-48 and Ti-MCM-48 cubic phased mesoporous materials by a two-step modification synthetic approach. High angle powder XRD studies indicate that the CdS and TiO_2 species can be well dispersed in the MCM-48 mesoporous materials since no peaks for bulk CdS or TiO_2 were found. Low angle XRD, TEM, and nitrogen physisorption studies indicate that the ordered cubic phase of Si-MCM-48 and Ti-MCM-48 was preserved after the introduction of CdS. All the studied samples showed photocatalytic hydrogen evolution under visible light irradiation even in the absence of Pt as a co-catalyst and sulfide and/or sulfite as sacrificial agents. The band edge positions of both CdS and TiO_2 dispersed in MCM-48 were estimated by UVPS studies. Time-resolved fluorescence emission decay study provided information regarding the kinetics of electron transfer rates from CdS to TiO_2. A clear correlation between the CdS content and photocatalytic activity was found. EPR studies confirmed the electron transfer from CdS to TiO_2; evident by the presence of Ti^{3+} under visible light irradiation. This study indicates that CdS-Ti-MCM-48-21-MPTMS-5 exhibits high efficiency, the apparent quantum yield of this material was found to be 24.8% even in the absence of Pt as a co-catalyst. In addition, the recycling study suggests that the stability of CdS in the CdS-Ti-MCM-48-MPTMS samples was significantly enhanced and the chemical loss of CdS after a long period photocatalytic reaction was less than 10%.

Acknowledgements

Thanks are due to NSF-CHE-0722632, NSF-EPS-0903804, DE-EE0000270, and SD NASA-EPSCOR NNX12AB17G. Use of the Center for Nanoscale Materials was supported by the U. S. Department of Energy, Office of Science, Office of Basic Energy Sciences, under Contract No. DE-AC02-06CH11357. We are thankful to Dr Phil Ahrenkiel at South Dakota School of Mines and Technology for assistance with TEM studies.

References

1 A. Fujishima and K. Honda, *Nature*, 1972, **238**, 37–38.
2 M. AshokKumar, *Int. J. Hydrogen Energy*, 1998, **23**, 427–438.
3 A. Kudo and Y. Miseki, *Chem. Soc. Rev.*, 2009, **38**, 253–278.
4 X. Chen, S. Shen, L. Guo and S. S. Mao, *Chem. Rev.*, 2010, **110**, 6503–6570.
5 T. Takata, A. Tanaka, M. Hara, J. N. Kondo and K. Domen, *Catal. Today*, 1998, **44**, 17–26.
6 F. E. Osterloh, *Chem. Mater.*, 2007, **20**, 35–54.
7 K. Maeda, *J. Photochem. Photobiol., C*, 2011, **12**, 237–268.
8 G. L. Chiarello, E. Selli and L. Forni, *Appl. Catal., B*, 2008, **84**, 332–339.
9 D. Y. C. Leung, X. L. Fu, C. F. Wang, M. Ni, M. K. H. Leung, X. X. Wang and X. Z. Fu, *ChemSusChem*, 2010, **3**, 681–694.
10 M. Kitano, M. Matsuoka, M. Ueshima and M. Anpo, *Appl. Catal., A*, 2007, **325**, 1–14.
11 M. Bandyopadhyay, A. Birkner, M. W. E. van den Berg, K. V. Klementiev, W. Schmidt, W. Grünert and H. Gies, *Chem. Mater.*, 2005, **17**, 3820–3829.

12 M. S. Morey, S. O'Brien, S. Schwarz and G. D. Stucky, *Chem. Mater.*, 2000, **12**, 898–911.
13 S. Yuan, L. Shi, K. Mori and H. Yamashita, *Mater. Lett.*, 2008, **62**, 3028–3030.
14 M. Anpo, H. Yamashita, K. Ikeue, Y. Fujii, S. G. Zhang, Y. Ichihashi, D. R. Park, Y. Suzuki, K. Koyano and T. Tatsumi, *Catal. Today*, 1998, **44**, 327–332.
15 M. Anpo, T.-H. Kim and M. Matsuoka, *Catal. Today*, 2009, **142**, 114–124.
16 A. Kudo, H. Kato and I. Tsuji, *Chem. Lett.*, 2004, 1534–1539.
17 K. Maeda, T. Takata, M. Hara, N. Saito, Y. Inoue, H. Kobayashi and K. Domen, *J. Am. Chem. Soc.*, 2005, **127**, 8286–8287.
18 K. T. Ranjit, R. Krishnamoorthy, T. K. Varadarajan and B. Viswanathan, *J. Photochem. Photobiol., A*, 1995, **86**, 185–189.
19 M. Sathish, B. Viswanathan and R. P. Viswanath, *Int. J. Hydrogen Energy*, 2006, **31**, 891–898.
20 Q. Li, B. D. Guo, J. G. Yu, J. R. Ran, B. H. Zhang, H. J. Yan and J. R. Gong, *J. Am. Chem. Soc.*, 2011, **133**, 10878–10884.
21 D. Meissner, R. Memming and B. Kastening, *J. Phys. Chem.*, 1988, **92**, 3476–3483.
22 T. Inoue, T. Watanabe, A. Fujishima, K.-i. Honda and K. Kohayakawa, *J. Electrochem. Soc.*, 1977, **124**, 719–722.
23 J. S. Jang, W. Li, S. H. Oh and J. S. Lee, *Chem. Phys. Lett.*, 2006, **425**, 278–282.
24 G.-S. Li, D.-Q. Zhang and J. C. Yu, *Environ. Sci. Technol.*, 2009, **43**, 7079–7085.
25 H. Yan, J. Yang, G. Ma, G. Wu, X. Zong, Z. Lei, J. Shi and C. Li, *J. Catal.*, 2009, **266**, 165–168.
26 S. Y. Ryu, W. Balcerski, T. K. Lee and M. R. Hoffmann, *J. Phys. Chem. C*, 2007, **111**, 18195–18203.
27 R. Peng, D. Zhao, J. Baltrusaitis, C.-M. Wu and R. T. Koodali, *RSC Adv.*, 2012, **2**, 5754–5767.
28 D. Zhao and Y. Wan, *Chem. Rev.*, 2007, **107**, 2821–2860.
29 R. Peng, D. Zhao, N. M. Dimitrijevic, T. Rajh and R. T. Koodali, *J. Phys. Chem. C*, 2012, **116**, 1605–1613.
30 D. Zhao, S. Budhi, A. Rodriguez and R. T. Koodali, *Int. J. Hydrogen Energy*, 2010, **35**, 5276–5283.
31 B. Boote, H. Subramanian and K. T. Ranjit, *Chem. Commun.*, 2007, 4543–4545.
32 Z. T. Zhang, S. Dai, X. D. Fan, D. A. Blom, S. J. Pennycook and Y. Wei, *J. Phys. Chem. B*, 2001, **105**, 6755–6758.
33 W. Xu, Y. T. Liao and D. L. Akins, *J. Phys. Chem. B*, 2002, **106**, 11127–11131.
34 S. Shen and L. Guo, *Mater. Res. Bull.*, 2008, **43**, 437–446.
35 Y. J. Zhang, L. Zhang and S. Li, *Int. J. Hydrogen Energy*, 2010, **35**, 438–444.
36 J. Yu, Z. Feng, L. Xu, M. Li, Q. Xin, Z. Liu and C. Li, *Chem. Mater.*, 2001, **13**, 994–998.
37 W.-S. Chae, J.-H. Ko, K.-H. Choi, J.-S. Jung and Y.-R. Kim, *J. Anal. Sci. Technol.*, 2010, **1**, 25–29.
38 H. Weller, H. M. Schmidt, U. Koch, A. Fojtik, S. Baral, A. Henglein, W. Kunath, K. Weiss and E. Dieman, *Chem. Phys. Lett.*, 1986, **124**, 557–560.
39 M. L. Steigerwald and L. E. Brus, *Annu. Rev. Mater. Sci.*, 1989, **19**, 471–495.
40 N. Herron, Y. Wang, M. M. Eddy, G. D. Stucky, D. E. Cox, K. Moller and T. Bein, *J. Am. Chem. Soc.*, 1989, **111**, 530–540.
41 G. Liu, W. Jaegermann, J. He, V. Sundström and L. Sun, *J. Phys. Chem. B*, 2002, **106**, 5814–5819.
42 X. Chen, L. Liu, P. Y. Yu and S. S. Mao, *Science*, 2011, **331**, 746–750.
43 M. Inokuti and F. Hirayama, *J. Chem. Phys.*, 1965, **43**, 1978–1989.
44 C. Lin, M. T. Berry and P. Stanley May, *J. Lumin.*, 2010, **130**, 1907–1915.
45 D. Dung, J. Ramsden and M. Graetzel, *J. Am. Chem. Soc.*, 1982, **104**, 2977–2985.
46 P. A. Sant and P. V. Kamat, *Phys. Chem. Chem. Phys.*, 2002, **4**, 198–203.
47 J. Z. Zhang, *J. Phys. Chem. B*, 2000, **104**, 7239–7253.
48 A. Kumar and A. K. Jain, *J. Mol. Catal. A: Chem.*, 2001, **165**, 265–273.
49 R. S. Dibbell and D. F. Watson, *J. Phys. Chem. C*, 2009, **113**, 3139–3149.
50 L. Spanhel, H. Weller and A. Henglein, *J. Am. Chem. Soc.*, 1987, **109**, 6632–6635.
51 S. M. Kuznicki, K. L. DeVries and E. M. Eyring, *J. Phys. Chem.*, 1980, **84**, 535–537.
52 A. Ghorbel, A. Tuel, E. Jorda, Y. Ben Taarit and C. Naccache, in *Studies in Surface Science and Catalysis*, ed. B. Laurent and K. Serge, Elsevier, 1995, vol. 97, pp. 471–476.
53 M. Engström, O. Vahtras and H. Ågren, *Chem. Phys. Lett.*, 2000, **328**, 483–491.